2015

Progress in resonator quantum well infrared photodetector (R-QWIP) focal plane arrays

Eric A. DeCuir Jr.
U.S. Army Research Laboratory, Adelphi, MD

Kwong-Kit Choi
U.S. Army Research Laboratory, Adelphi, MD

Jason Sun
U.S. Army Research Laboratory, Adelphi, MD

Priyalal S. Wijewarnasuriya
U.S. Army Research Laboratory, Adelphi, MD

Progress in resonator quantum well infrared photodetector (R-QWIP) focal plane arrays

CrossMark

Eric A. DeCuir Jr. *, Kwong-Kit Choi, Jason Sun, Priyalal S. Wijewarnasuriya

U.S. Army Research Laboratory, RDRL-SEE-I, 2800 Powder Mill Road, Adelphi, MD 20783, United States

HIGHLIGHTS

- We report on the performance of a 640×512 resonant quantum well infrared photodetector (R-QWIP) focal plane array (FPA).
- We report on the conversion efficiency and quantum efficiency as a function of bias and temperature.
- We report on the dark current and Noise Equivalent Temperature Difference as a function of bias and temperature.

ARTICLE INFO

ABSTRACT

In this work, the performance of a 640×512 long-wavelength resonant quantum well infrared photodetector (R-QWIP) focal plane array (FPA) was evaluated as a function of operating temperature, bias, and photon flux using an F/2.2 optic. From these FPA measurements an assessment of the dark current, noise, conversion efficiency and noise-equivalent temperature difference is provided herein. Histogram results are used to support a statistical interpretation of operability and non-uniformity across the R-QWIP FPA. In addition, single pixel devices fabricated from the same wafer lot enabled supplemental noise gain and spectral response measurements. The spectral response of this R-QWIP structure was confirmed to peak around 8.3 microns with a spectral bandwidth or approximately 1 micron (full-width half maximum) and the noise gain measurements were used to provide an estimation of the expected external quantum efficiency (conversion efficiency = quantum efficiency $*$ gain).

Published by Elsevier B.V.

1. Introduction

Quantum engineering of heterostructures such as quantum wells and superlattices have progressed greatly since first proposed more than four decades ago by Esaki and Tsu [1]. Monopolizing upon this proposed idea and increased maturity of the III–V material system, the quantum well infrared photodetector (QWIP) was finally realized [2]. In parallel with the success and limitations of III–V AlGaAs/(In)GaAs QWIP technology, the infrared (IR) research community has also maintained an interest in other III–V technologies such as InAs/(In)GaSb type-II strained layer superlattices (SLS) and InAs/InAsSb Ga-free materials [3,4]. However, to address the perceived limitations of first generation QWIP technology, Choi et al. has provided new modeling and fabrication techniques in diffractive element and resonant structure design to further push the boundaries of QWIP performance [5–8]. The

advances of Choi's three-dimensional finite element electromagnetic (EM) modeling techniques offer theoretical simulations of new high performance QWIP designs and provide an transferable framework that makes this resonator technology accessible to other existing detector technologies. The verified consistency of Choi's theoretical model coupled with the maturity and accessibility of III–V technology provide an invaluable resource to both researchers and industry alike.

In this work, experimental verification of the first fabricated resonator-QWIP or R-QWIP FPA is provided herein. The ultimate goal of this design (from a FPA perspective) was to provide a QWIP platform that could enable shorter integration times applicable to high speed imaging. This decrease in integration time is directly connected to the enhanced conversion efficiency of the RQWIP over typical QWIP designs. This resonator structure is designed to boost the photon absorbing efficiency through the addition of a resonant cavity and metallic diffractive elements that effectively confines and steers the fundamental polarization component responsible for photon absorption in the plane of the quantum well

---

absorber, respectively. In essence, this resonant enhanced electron–photon coupling scheme successfully boosts the conversion efficiency, thereby mandating shorter integration times (exposure times) than competing QWIP designs (grating or corrugated designs). Herein, only experimental results detailing the performance of a 640 × 512 FPA will be presented. Explicit details relating to the theoretical modeling of designs and fabrication will be reserved for complementary papers at the 2014 Quantum Structured Infrared Photodetector International Conference (authors: Choi and Sun, respectively).

2. Materials and methods

2.1. Experimental details

An R-QWIP FPA hybridized to an Indigo ISC9803 read-out integrated circuit (ROIC) was evaluated to provide a quantitative understanding of the pixel-to-pixel performance of a 640 × 512 array. In this study, dark current, conversion efficiency (C.E.), quantum efficiency (Q.E.), and Noise Equivalent Differential Temperature (NEdT) was investigated versus bias and temperature. The data collection methodology consisted of 32 contiguous 640 × 512 frames for each particular bias, scene, or temperature. These 32 frames were subsequently reduced into a single 640 × 512 mean/average frame. Hereafter, the notation for the resultant 640 × 512 mean/average frame will be noted as either dark or illuminated respectively as follows: $\overline{N}_{dark}$ or $\overline{N}_{25C}$, where the lower notation specifies the condition of illumination (dark or blackbody temperature). Additionally, the standard deviation of this 32 frame-set also offered access to the temporal noise frame at each condition. The notation for this frame will follow the aforementioned nomenclature, e.g. σ_{dark} or σ_{25C}. These mean and noise frames were used in the calculations of dark current, C.E./Q.E. and NEdT. Furthermore, the population distributions of these mean frames are reported as histograms, from which statistics relating to operability and non-uniformity are derived.

In addition to a 640 × 512 FPA, supplementary 40 × 40 element fan-out structured test arrays were also fabricated for evaluation of spectral response and noise gain. These 1600 elements were tied together in parallel to promote increased signal-to-noise for these measurements. The spectral response and noise gain (g) acquired from these test devices as a function of bias are shown in Fig. 1. Experimental finding acquired from these studies are utilized herein, but details pertaining to the measurement of these hybridized test structures are not within the scope of this paper and are provided in Choi et al. [6].

2.2. R-QWIP structure and pixel details

In this R-QWIP FPA, a 25-μm pixel pitch was adopted to comply with a commercially available Indigo ISC9803 read-out integrated circuit (ROIC). The final fabricated pixel size, shown in Fig. 1 is 22.2 μm × 22.2 μm with an effective area of approximately 4.93×10^{-6} cm^2. The diffractive element design utilized for each pixel consisted of an array of GaAs square rings, which are also shown in Fig. 1 as both designed and fabricated. In effort to maximize the Q.E., the diffractive element geometry and pitch was optimized through electromagnetic modeling [7]. The QWIP material structure consisted of a 21 periods of (4.8 nm GaAs/ 50 nm Al$_{0.242}$Ga$_{0.758}$As) quantum well structure with a total absorber thickness of approximately 1.15 μm. Quantum wells were doped to a nominal doping density of 1×10^{18} cm^{-3}. Since the quantum well absorber thickness is fixed, to tune the desired resonant condition within the pixel, the thickness of the ground contact was used to optimize the resonant cavity volume.

2.3. Test dewar

The packaged FPAs were epoxy mounted onto an 84-pin LCC and various bias and signal lines were wire bonded out for connectivity into a continuous flow Lakeshore modular test dewar (MTD150) with individually shielded coaxial break-outs for each LCC pin. The dewar was equipped with a 2-inch KRS-5 window yielding approximately 69.5% transmission over the spectral range of interest (6–10 microns). All measurements were carried out within this MTD150 dewar utilizing an in situ cold stop to provide a zero field-of-view (FOV) for dark current measurements and a F/2.2 FOV for radiometric measurements. The calibrated flux density for these radiometric measurements was delivered by a 4 inch^2 CI Systems extend area blackbody (emissivity $\sim$ 0.99) which was closely abutted to the test dewar window during measurements such that uniform illumination filled the FPA FOV.

### 2.4. Dark current measurement technique

The dark current of this R-QWIP was measured at temperatures 50 and 58 K and biases of 1, 2, 2.5, and 3 v. To get a more accurate interpretation of the dark current at these specified conditions, collected dark charge was measured as a function of integration time at each bias point and temperature. The statistical average of a 32 contiguous frame-set ($\overline{N}_{dark}$) is then further reduced into a single mean data point derived from this reduced dark frame ($\overline{N}_{dark}$). The amassed collection of these data points are then plotted as the mean collected dark signal (e-) versus integration time (s). A representation of the dark current (electrons/s) is then derived from the slope of the dark signal versus integration time. The added benefit of extracting the dark current utilizing this technique arises from the fact that any non-linearity in the ROIC over the well capacity's dynamic range will instantly be revealed. In the case of this ISC9803 ROIC, it was shown that a non-linearity in the ROIC gain occurred at a transition point of approximately 1.3 million electron (Me-) or 11.6% of the 11.2 Me- dynamic range. In this study, this transition point is used to define a high gain regime (<1.3 Me-) and low gain regime (>1.3 Me-). Further details regarding this phenomenon will be discussed in the dark current data analysis section.

### 2.5. Conversion efficiency and quantum efficiency

The measured spectral response from the aforementioned 40 × 40 test device is utilized to calculate the effective in-band incidence (ϕ_p [photons s^{-1} cm^{-2}]) provided by an extended area blackbody (BB) where the spectral band-pass of the detector is non-zero. The derivation of the in-band incidence is facilitated via a multiple Lorentzian fit of the normalized spectral response to form a functionally equivalent response as a function of wavelength ($R(\lambda)$[μm]) as shown in Fig. 2. The convolution of this spectral response ($R(\lambda)$) with Plank's blackbody spectral exitance $M_p(\lambda, T_{BB})$ ([photons s^{-1} cm^{-2} μm^{-1}]) (shown on the second y-axis of Fig. 2) integrated over the spectral band-pass (λ_{short} to λ_{long}), multiplied by the KRS-5 window transmission (T_w(%)), and the solid angle/π (Ω_d/π) provides the effective in-band incidence (or photon flux) expression shown in Eq. (1):

$$\Phi_p = T_w \cdot \frac{\Omega_d}{\pi} \int_{\lambda_{short}}^{\lambda_{long}} R(\lambda) \cdot M_p(\lambda, T_{BB}) d\lambda \, [photons \; s^{-1} \; cm^{-2}] \qquad (1)$$

M_p is simply Planks law for spectral exitance from ideal blackbody source with an emissivity of 1. Due to the relatively narrow band nature of the RQWIP response, the FPA was measured in the absence of a narrow-band filter. Since there is no narrow-band filter to provide specific narrow band irradiance to the detector, the
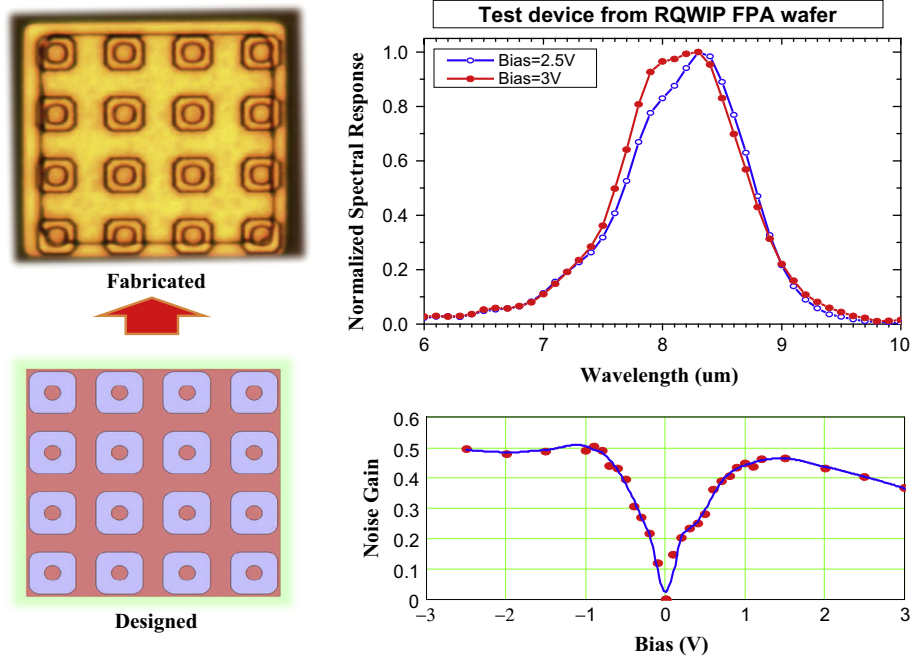
Fig. 1. (a) Illustration of a single pixel's designed and fabricated diffractive elements used in this RQWIP design. (b) Normalized spectral response of RQWIP test array at 2.5 V and 3 V. Note: Spectral shape of 2.5 V is conserved at 1 V and 2 V.
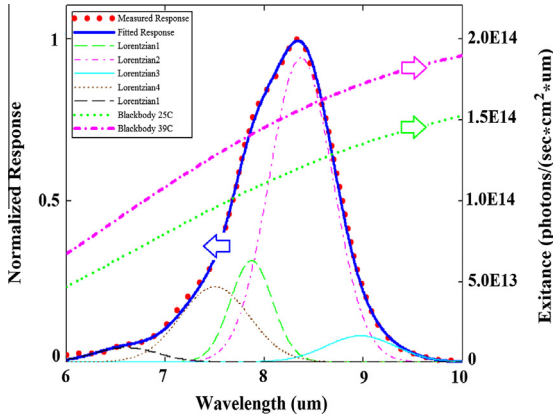
Fig. 2. Normalized spectral response of RQWIP test array at 2.5 V with multiple Lorentzian fit used to develop a functional equivalent for the measured spectral response.

normalized spectral response curve is used to sensitize the wavelength dependent blackbody spectral exitance to the wavelength spectral sensitivity of the detector. That is, since the detector only responds to a specific in-band flux with varying degrees of sensitivity in its unique band-pass, this technique accounts for the proportional sensitivity of the detector and photon exitance at each wavelength. Consequently, this calculated effective in-band incidence is later used to calculate the peak conversion efficiency (C.E.) of this R-QWIP FPA. The C.E. is simply the product of the noise gain (g) and quantum efficiency (Q.E. or η), i.e., C.E. = $g * \eta$. In this investigation, the noise gain measured in fan-out test devices is used to estimate the quantum efficiency of the FPA. This technique is similar to that described for responsivity by Levine et al. [10].

In order to accurately access the conversion efficiency of the FPA, one must accurately determine the ratio of photo-generated electrons to the number of photons striking the detector over a given time period. In the case of an FPA under background illumination, the total electron number ($\overline{N}_{25C}$ (e-)) collected over a specified

integration time arises from both dark and photon related mechanisms, i.e., $\overline{N}_{25C} = \overline{N}_{dark} + \overline{N}_{photo}$ ($\overline{N}_{dark}$ = dark electrons, $\overline{N}_{photo}$ = photo – electrons). These mechanisms referred to as both the dark current (I_{dark}) and photocurrent (I_{photo}) are related to the electron quantities ($\overline{N}_{dark}, \overline{N}_{photo}$) for a given integration time as follows below:

$$I_{dark} = qg_{thermal}g \Rightarrow \overline{N}_{dark} = \frac{I_{dark}\tau_{int}}{q} \tag{2}$$

$$I_{photo} = q\eta\Phi_p A_d g = C.E.(q\Phi_p A_d) \Rightarrow \overline{N}_{photo} = \frac{I_{photo}\tau_{int}}{q} \tag{3}$$

where q is the electron charge, $g_{thermal}$ is the thermal generation, g is the photoconductive gain, τ_{int} is the integration time, η is the quantum efficiency, A_d is the detector area, $\overline{N}_{dark}$ is the number of dark electrons, $\overline{N}_{photo}$ is the number of photo-generated electrons, and C.E. is the conversion efficiency. As seen in Eq. (3), the conversion efficiency is directly proportional to the product of the gain and quantum efficiency, which may be further related to the measured photocurrent by taking into account the specific in-band flux (ϕ_p) and area of the detector (A_d). Therefore, a direct measurement of the conversion efficiency is made possible by extracting the photo-generated electrons from the total electrons ($\overline{N}_{25C}$) collected over a specific integration time. However, since $\overline{N}_{25C}$ is explicitly coupled to the dark and photocurrent mechanisms, in order to isolate pure photocurrent, one must either have knowledge of the dark current or operate in a regime where $\overline{N}_{photo} >> \overline{N}_{dark}$ such that the dark current contribution is negligible. While the latter is readily achievable by operating at a low enough temperatures, removal of the dark current contribution via a differential technique is commonly adopted such that C.E. extraction is possible for a range of photo current to dark current ratios ($\overline{N}_{photo}/\overline{N}_{dark}$) greater than 1. The differential technique utilized in this study is given in Eq. (4):

$$C.E. = \eta * g = \frac{\Delta\overline{N}_{39C,25C}}{\Delta\Phi_p^{39C,25C}A_d\tau_{int}} = \frac{(\overline{N}_{photo}^{39C} - \overline{N}_{photo}^{25C})}{(\Phi_p^{39C} - \Phi_p^{25C})A_d\tau_{int}} \tag{4}$$
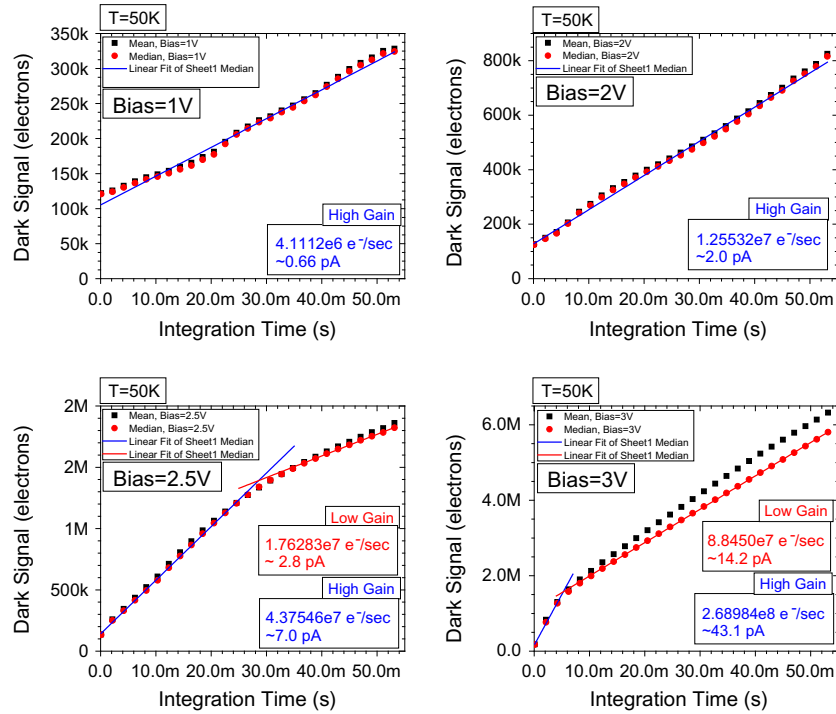
Fig. 3. Bias dependence of dark signal versus integration time for an R-QWIP FPA at 50 K. The fitted slope of the mean data provides the dark current at each bias. Non-linearity in the ROIC gain is supported in 2 and 2.5 V data as evidence by the two different slopes below and above 1.3 Me- well fill.
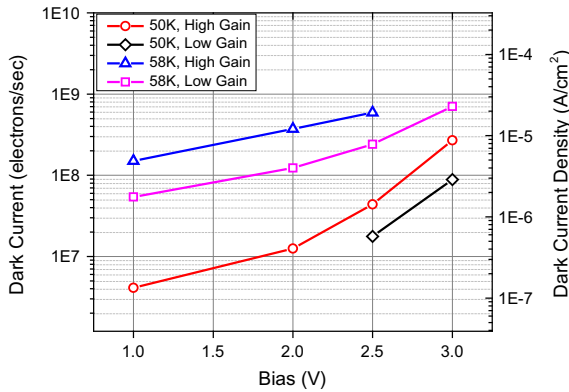
Fig. 4. Summary of the dark current (e⁻/s) and dark current density (A/cm²) versus bias for 50 and 58 K.

where $\Delta\overline{N}_{39C,25C}$ is the difference in total illuminated signals at 39 °C and 25 °C, $\Phi_p^{39C,25C}$ is the difference in the photon flux at 39 °C and 25 °C, A_d is the detector area, and τ_{int} is the integration time. When utilizing this technique, explicit knowledge of the explicit detector dark current is not required due to the invariability of dark current at a fixed FPA temperature and under different photon fluxes. In this regard, since each illuminated frame contains both photo and dark current, (e.g., $\overline{N}_{photo} = \overline{N}_{dark} + \overline{N}_{photo}$) the detector dark current component in the numerator of Eq. (4) will cancel and the difference of the total collected electrons at two different fluxes consist of only the difference in photocurrent. Therefore, both the C.E. and Q.E. for an FPA may be obtained by collecting a series of frames at two incremental fluxes and calculated as given in Eq. (4). Herein, all reported values of C.E. and Q.E. were calculated according to Eq. (4) at blackbody temperatures of 25 °C and 39 °C

2.6. Noise Equivalent Temperature Difference (NEdT)

The NEdT (also commonly referred to as NETD and NEΔT) is a figure of merit used to describe the sensitivity of a tactical infrared sensor and is defined as the smallest temperature difference that can be detected by that infrared sensor. This criteria is met when the temporal noise of the sensor is equal to the signal, i.e., Signal-to-Noise (S/N) = 1. In this study, the NEdT for an R-QWIP focal plane array is measured as a function of bias and at temperatures 50 K and 58 K. Experimentally the NEdT versus bias and temperature was calculated from a 25 °C and 39 °C scene as follows:

$$NEdT = \frac{\Delta T}{S/N} = \frac{\Delta T \sigma_{25C}}{\overline{N}_{39C} - \overline{N}_{25C}} \tag{5}$$

where σ_{25C} is the temporal noise of the 25 °C frame, $\overline{N}_{39C}$ is the signal collected at a 39 °C blackbody temperature, and $\overline{N}_{25C}$ is the signal collected at a 25 °C blackbody temperature. To enhance our understanding of the fundamental limitation of the detector material coupled with a limited amount of ROIC noise, the temporal limited NEdT [9] was also calculated as follows:

$$NEdT = \frac{1}{C_{ratio}} \sqrt{\left(\frac{2gN_{total} + Noise_{ROIC}^2}{N_{total}^2}\right) * \left(1 + \frac{N_{dark}}{N_{photo}}\right)^2} \tag{6}$$

where C_{ratio} is the contrast ratio, $Noise_{ROIC}$ is the ROIC noise, g is the photoconductive gain, N_{total} is the total collected electrons, N_{dark} are the dark electrons, and N_{photo} are the photo-electrons. These values were calculated from the available experimental data and compared to the experimentally measured NEdT. A full comparative analysis is given in the NEdT results section.

3. Results and discussion

Note: During testing of this FPA, it was observed that a number of rows and columns were inoperable after cool down cycle. These were excluded from the analysis and the effective format of the FPA considered in the subsequent results is 636×495.
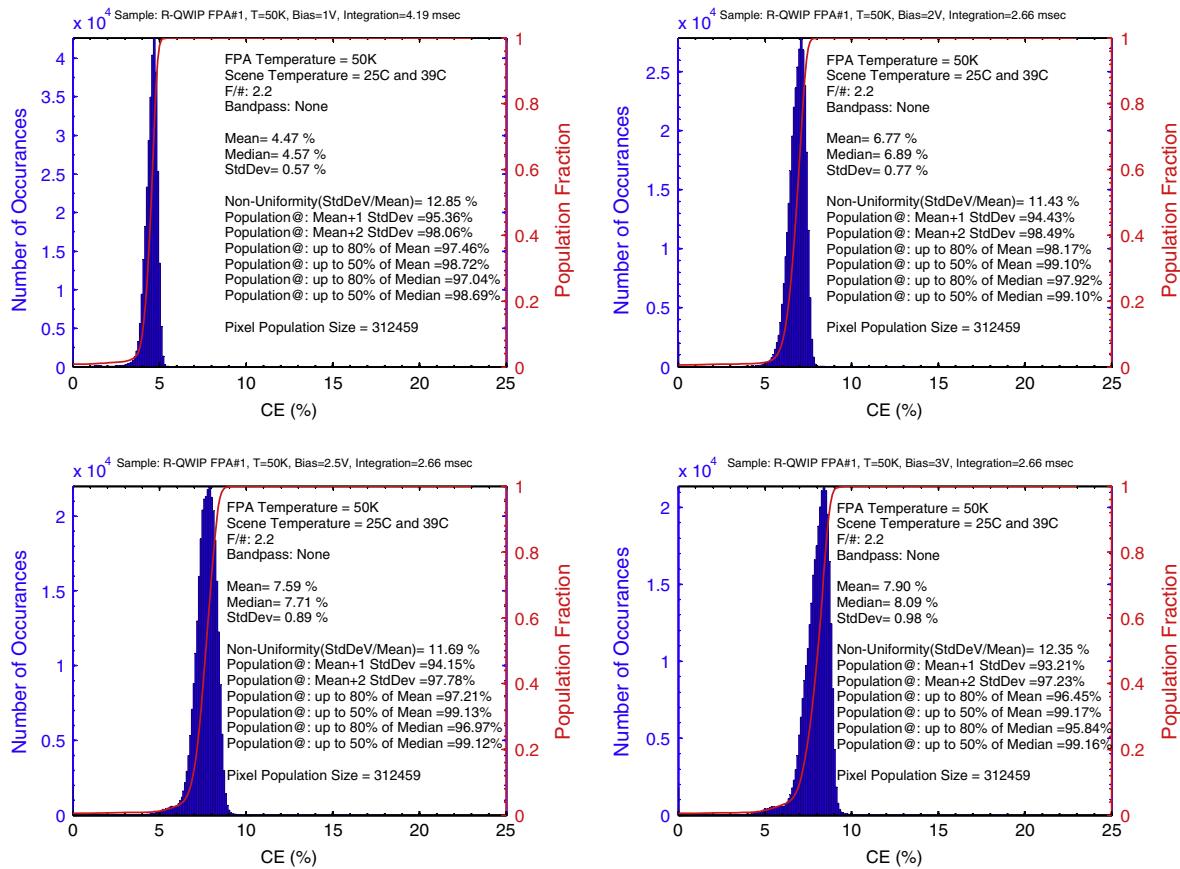
Fig. 5. Histograms of the conversion efficiency (C.E.) for an R-QWIP FPA at 50 K and at biases of 1 V, 2 V, 2.5 V, and 3 V. Statistics dictate population percentage skewed to the left of the mean, e.g., Population @: up to 80% of Mean includes all pixels with a C.E. up to 80% of the mean.

3.1. Dark current results

The dark current of an R-QWIP FPA was investigated at 50 and 58 K and at biases of 1, 2, 2.5, and 3 V. As mentioned previously in the experimental methods section for dark current analysis, the FPA was operated in a condition where an internal cold shield provided a zero FOV while dark signal was collected at various integration times. At 50 K, the dark signal (e⁻) as function of integration time and bias is shown in Fig. 3. To obtain the dark current, the reduced mean data from the FPA are fit with a linear expression to determine the overall slope of the data with increasing integration time. This slope is effectively the dark current in units of electrons/s. The dark current is expected to be proportional to the bias voltage since the increasing electric field enhances the probability of dark electron capture, whose source originate from thermionic and tunneling processes into the continuum. This effect is indeed observed in the measured dark current as it readily increases with increasing bias. The dark current at each bias is reported under each bias condition in Fig. 3, however, an observed non-linearity in the ROIC gain at both 2.5 V and 3 V required two independent linear fits to best represent the data. This effect does not fully present itself until the bias was greater than 2 V since the maximum well fill does not approach this gain transition point seen in 2.5 V and 3 V. This gain transition point was determined to be a condition of well fill that occurred at approximately 11% of the maximum dynamic range or 1.3 Me- (Max well: 11.2 Me-). Therefore, the overall gain of the ROIC has been divided into both a high and low gain regime, where low gain is greater than 1.3 Me- fill and high gain is lower than 1.3 Me- well fill. Of course, the dark current is not a condition of well fill and the reported

differences shown in Fig. 3 are only a consequence of non-linearity in the ROIC gain. During measurements, this non-linearity is best avoided by operating in the low gain regime (>1.3 Me-), where the remaining 89% of the dynamicrange is linear. A similar exercise was performed for 58 K, which exhibited elevated dark current due to the higher temperature of the FPA. The 58 K dark signal (e-) versus integration time (s) at 1, 2, 2.5, and 3 V as shown in Fig. 3 is omitted for brevity; however, a summary of the dark current at both 50 K and 58 K is presented in Fig. 4. Due to the elevated dark current at 58 K, most of the biases allowed access to both high gain and low gain regime values since both slopes were accessible in the integration sweep window. This dark current was further used for calculations of NEdT. Only the low gain regime is valid since the total well fill exceeded 1.3 Me-. The temporal NEdT values were not calculated for those biases and temperature where low gain regime was unknown. This analysis is later presented in Section 3.3.

3.2. Conversion efficiency and quantum efficiency results

The main attribute of this R-QWIP FPA is the enhancement of C.E. by utilizing a resonant cavity coupled with a diffractive element to trap and redirect incoming photons such that multiple passes of properly polarized light have the opportunity to be absorbed. The necessity of these multiple passes are linked to the physics of quantum wells that necessitate optimized balance of quantum well number (absorber thickness) and doping density to overcome the limitation of shorter majority carrier lifetimes (which in essence limit collection efficiency and temperature). Furthermore, the fact that QWIP are inherently extrinsic photoconductors and are
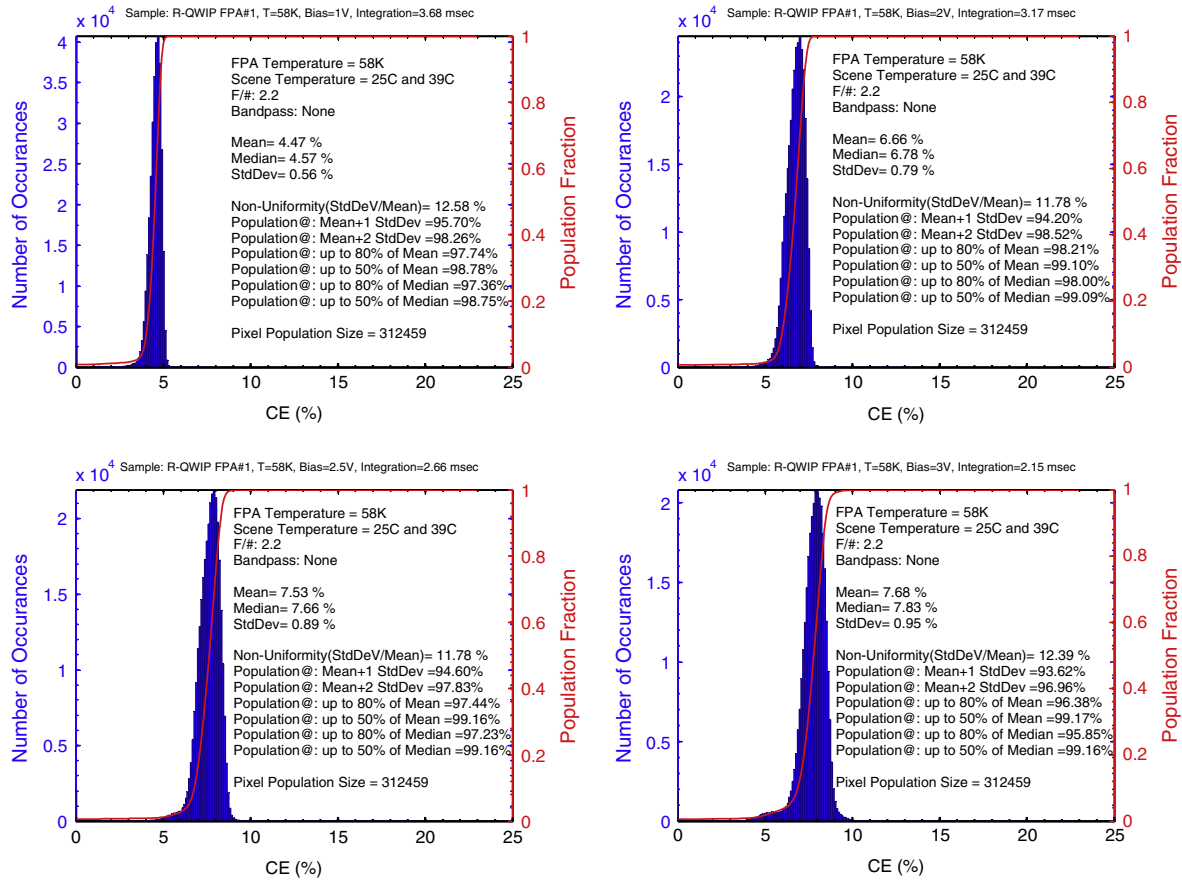
Fig. 6. Histograms of the conversion efficiency (C.E.) for an R-QWIP FPA at 58 K and at biases of 1 V, 2 V, 2.5 V, and 3 V. Statistics dictate population percentage skewed to the left of the mean, e.g., Population @: up to 80% of Mean includes all pixels with a C.E. up to 80% of the mean.

majority carrier devices, the absorption coefficient is directly proportional to the impurity level in the absorptive layers. Given that the dark current is also directly proportional to this doping density, a delicate balance between doping density, absorption coefficient, and quantum well number must be achieved to optimize the efficiency of the device. The benefit of a resonant cavity, multi-pass QWIP structure is an increase in the effective optical path length perpendicular to the direction of carrier collection. That is, the effective lateral width of the quantum well layer is increased without compromising the collection efficiency of the device since the carrier transit time (thickness(t)/drift velocity (V_{drift}, $V_{drift} = \mu_e E$) is unaffected. The bias dependent C.E. is merely a consequence of this 21 quantum well, bound-to-continuum QWIP design. Since conversion efficiency is the product of the overall quantum efficiency and the photoconductive gain, it can be shown that the C.E. is dictated by both the overall absorption efficiency of the quantum well layer (dependent on both doping and number of quantum wells, i.e., thickness) as well as the applied voltage. The voltage dependence

is a consequence of the photoconductive gain (g) which is a function of majority carrier lifetime (τ_e), majority carrier mobility (μ_e), bias voltage (V), and well thickness (t) as follows: $g = \tau_e * \mu_e * V/t^2$. The interplay between well thickness, gain, and applied bias voltage are key parameters that typically limit traditional QWIP design. However, the addition of a resonant cavity relaxes the well thickness requirements since increased absorption is promoted via multiple passes through the absorptive region. In essence, this enables designs that operate at lower biases to achieve similar gain factors yet also maintain quantum efficiency with a reduced number of quantum wells. The detailed physics related to traditional QWIP bias-dependent nature have been well documented and understood for many years [10] and will not be discussed herein.

The main focus of this section will be to discuss the statistical distribution of the histograms as they relate to both temperature and bias. The bias dependent conversion efficiency at both 50 and 58 K was calculated as described in Section 2.5. Detailed histograms providing the imager's performance are shown in Figs. 5 and

Table 1
Resonator-QWIP measured values of conversion efficiency (C.E.), quantum efficiency (Q.E.), Gain, and measured Noise Equivalent Temperature Difference (NEdT) as compared with temporal limited NEdT and system noise corrected NEdT. Note: Q.E. was extrapolated from Gain and C.E., i.e., C.E. = Gain * Q.E.

Bias (V)	Gain	Mean C.E. (%)		Mean Q.E. (%)		Measured NEdT (mK) [Mean]		Temporal limited NEdT (mK)[*]		System Noise Corrected NEdT (mK) [Mean][**]	
		T = 50 K	T = 58 K	T = 50 K	T = 58 K	T = 50 K	T = 58 K	T = 50 K	T = 58 K	T = 50 K	T = 58 K
1.0	0.441	4.47	4.48	10.14	10.16	42.72	47.49	#NA	25.26	25.38	28.22
2.0	0.436	6.77	6.67	15.53	15.30	44.24	40.81	#NA	22.66	26.11	24.46
2.5	0.404	7.59	7.54	18.79	18.66	44.54	47.13	21.95	22.98	23.57	24.69
3.0	0.365	7.90	7.68	21.64	21.04	179.47	59.93	20.15	25.23	21.66	26.92

[*] Temporal Noise limited NEdT, ROIC noise = 500 e⁻, Contrast ratio = 1.57 e⁻².
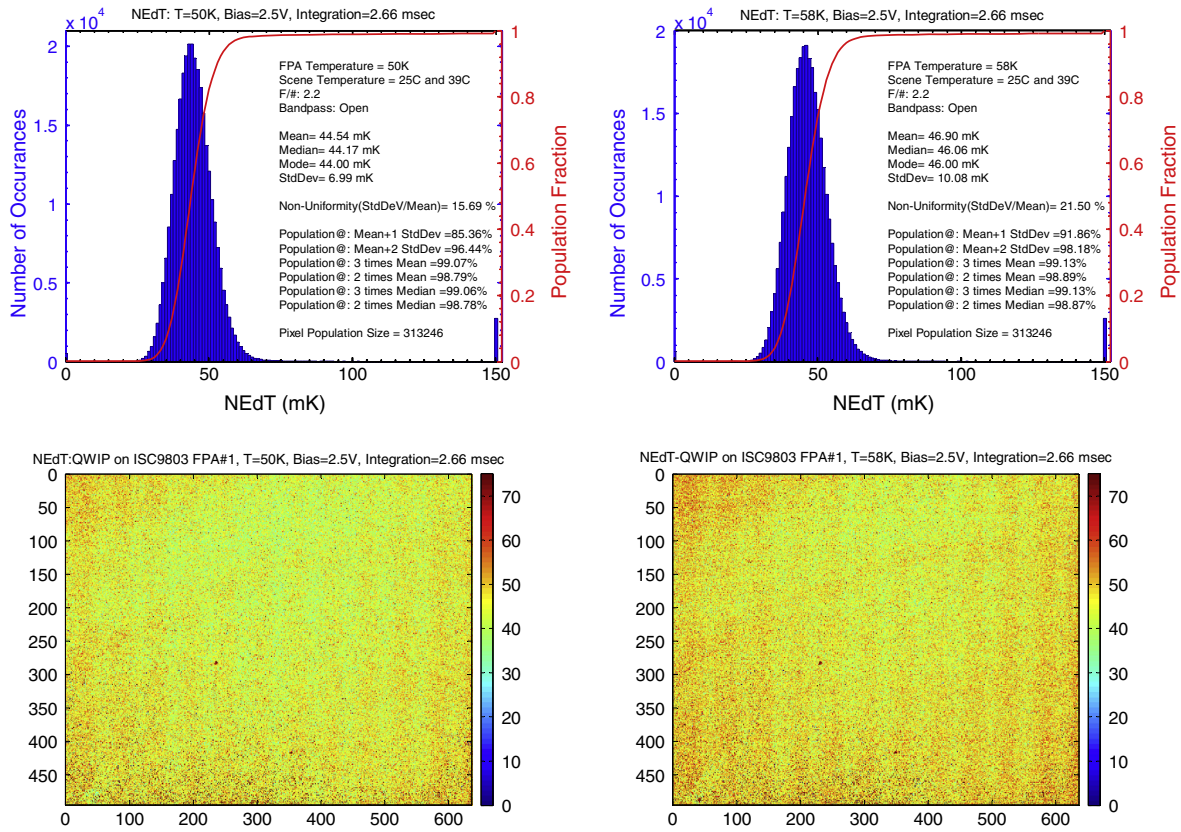[**] Measured NEdT with additional extrapolated system noise removed.

Fig. 7. Histograms and Images of the Noise Equivalent Differential Temperature (NEdT) for an R-QWIP FPA at 50 and 58 K at a bias of 2.5 V. Statistics dictate population percentage skewed to the right of the mean, e.g., Population @: 2 times mean includes all pixels with a NEdT up to twice the mean.

6. The integration times selected for these studies were the result of maintaining at 50% well fill or greater at the lowest flux provided to the FPA (flux at 25 °C). It is also important to note that no non-uniformity correction (NUC) has been performed to correct the data in this study. Therefore, some inflation of non-uniformity and uniformity metrics are expected since some moderate cosine[4] effects were present with this F/2.2 optic. The non-uniformity (standard deviation (σ)/mean (μ)) of the R-QWIP FPA at 50 and 58 K appear to be relatively consistent with both temperature and bias and stay within the range of 12–13%. The operability of the FPA is dictated by a left skew of the pixel response toward

lower C.E. and the total pixel population up to a percentage of the mean or median value is used to quote the operability. While multiple metrics are available in both Figs. 5 and 6, one may focus on a single metric to judge this operability with applied bias. In this regard, observing the entire population of pixels having at least 80% of the median C.E. shows that a peak operability of 97.9% is obtained at 2 V at 50 K and 98.0% at 58 K, however, the C.E. of the FPA at a 2V bias is only 86.7% of the maximum C.E. obtained at 3V. Operating at this higher bias appears to drop the operability to 95.8% and 95.9% at 50 K and 58 K respectively. This is also evidenced by the increasing population witnessed in the tails of the
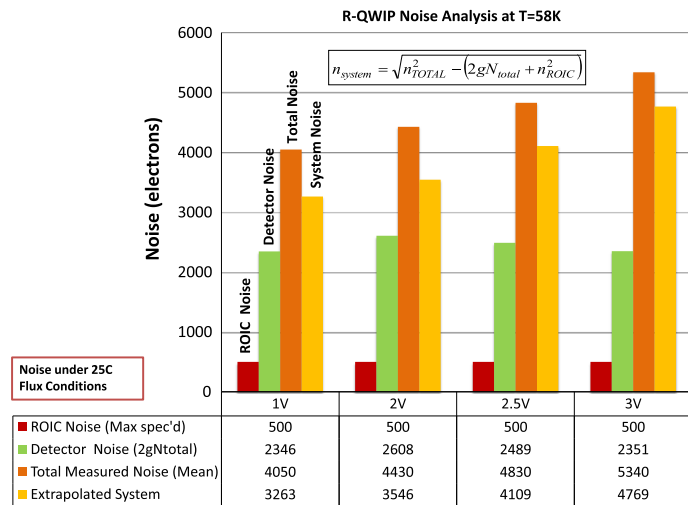

Fig. 8. Bar graph of Noise components used to extrapolate excess noise in experimental test setup.

Table 2
A list of noise figures versus biases that were used in the calculation of excess system noise. This includes FPA noise (both detector and expected ROIC noise of 500 electrons) and measured total noise. The photo-electron (N_{photo}) to dark-electron ratio (N_{dark}) is also provided as a key metric affecting the temporal NEdT (see Eq. (6)).

Bias (V)	FPA noise (detector and ROIC Only) (e^-)		Deduced sytem noise (e^-)		Total measured noise (e^-)		Np/Nd 25C background	
	$T = 50$ K	$T = 58$ K	$T = 50$ K	$T = 58$ K	$T = 50$ K	$T = 58$ K	$T = 50$ K	$T = 58$ K
1.0	2448	2399	3302	3263	4110	4050	#NA	30.4
2.0	2406	2655	3332	3546	4110	4430	#NA	19.2
2.5	2458	2539	3947	4109	4650	4830	152.1	11.0
3.0	2475	2403	21,055	4769	21,200	5340	33.3	4.0

distributions with increasing bias. While this tail is more pronounced as the bias increases, no evidence is foretelling the nature of this tail with increasing temperature. A more detailed study of the temperature dependent nature is definitely needed before any conclusions may be made about the nature of this tail with increasing temperature. However, it can be concluded that while voltage is enhancing the effective C.E. of the array, a number of pixels shift into a low responding tail in the distribution. A continued study of additional R-QWIP FPAs is forthcoming to help understand if these higher electric field effects are material or possibly ROIC related. A summary of the mean C.E. versus bias and the calculated Q.E. based on the photoconductive gain obtained in test device studies is given in Table 1.

3.3. Noise Equivalent Temperature Difference (NEdT)

The NEdT was experimentally calculated as detailed in Section 1.5 and compared to the temporal limited NEdT that was expected from this R-QWIP limited only by the detector and ROIC noise. The mean values for these experimental and temporal limited NEdT values are given in Table 1. In the case of the temporal limited NEdT, a maximum ROIC noise of 500 electrons was based on the maximum expected noise given in the ROIC documentation. In an effort to simply this discussion, only the histograms of the 2.5 V NEdT at 50 and 58 K are provided in Fig. 7 along with the NEdT image to help illustrate an obvious limitation in the measurement. A similar statistical treatment is performed with the NEdT histograms with the exception that histogram skew tends toward the right of the distribution (toward higher NEdT values). Hence the operability is quoted as the population of pixels that are twice the median NEdT, which yields an operability of 98.8% at 50 K and 98.9% at 58 K. The non-uniformity of the NEdT at 2.5 V and temperatures 50 and 58 K show unexpected change with temperature as this was not the case in the C.E. measurements (granted that the C.E. measurement is not explicitly noise contingent like NEdT). Note that the NEdT images also appear to reveal a fixed pattern noise that appears elevated at 58 K. Given that only the temperature is changed in these NEdT images at a 2.5 V bias, leads one to believe that this may be a temperature induced skew in the histogram toward larger NEdT values. While this effect seems probable, one would hesitate to consider this as rigorously conclusive evidence given the limited data set. Nonetheless, a more pressing issue is the elevated NEdT as compared to the temporal limited NEdT shown in Table 1.

Comparison of the experimental and temporal limited NEdT shows that a large discrepancy exists between what should be expected with no additional noise beyond detector and ROIC noise. As seen in Table 1, the measured NEdT is approximately double that of the temporal limited case leading one to believe that a large source of excess system noise is present in the measurement. In an effort to better understand the excess system noise, a simple extraction of excess noise is performed as shown in Fig. 8. In this exercise, one may easily account for noise generated from the detector $(n_d = \sqrt{2gN_{total}^{25C}})$, expected noise from the ROIC ($n_{ROIC} = 500$ electrons), and the actual measured noise (n_{total} based

on bias and temperature). From these known/expected values, one may extract the excess system noise as follows in equation:

$$\left(n_{system} = \sqrt{n_{total}^2 - \left(2gN_{total}^{25C} - n_{ROIC}^2\right)}\right) \tag{7}$$

A summary of the calculated excess system noise is given in Table 2, which was subsequently removed from the experimentally collected noise used to calculate NEdT. This system noise corrected NEdT is provided in Table 1 and provides a more reasonable correlation to the temporal NEdT. Therefore, it can be confidently concluded that the presence of a unknown excess noise source has effectively coupled into the NEdT measurement, thereby approximately doubling the expected NEdT. The origin of this excess noise source is under investigation. The photocurrent to dark current ratio is also provided in Table 2. The degradation in this ratio is due to increasing dark currents at higher temperatures/biases. At elevated temperatures, the dark current begins to compromise the dynamic range of the well capacity as it further confiscates an appreciable portion of the well fill, thereby leaving less capacity for photocurrent. This in essence begins to compromise the sensitivity of your detector at low fluxes.

4. Conclusion

The performance of the first produced R-QWIP FPA was evaluated as function of temperature and bias to reveal performance metrics relating to dark current, conversion efficiency(C.E.)/quantum efficiency (Q.E.), and noise equivalent difference temperature (NEdT). It was shown that the dark current of the R-QWIP FPA exhibited both a bias and temperature dependence and nearly an order increase in dark current was observed from 50 K to 58 K. The dark current experienced in this R-QWIP having a peak response of 8.3 μm correlates well with expected dark currents in similar QWIP structures [9,10]. The conversion efficiency/(quantum efficiency) of this R-QWIP, which had negligible change with temperature from 50 to 58 K, increased with bias from approximately 4.5%/(10.1%) to 7.9%/(21.6%) at 1 and 3 V respectively, thereby confirming the efficacy of this resonant structure. It was also shown that by observing the entire population of pixels having at least 80% of the median C.E. reveals an operability of 97.9% at 2 V (50 K) and 98.0% (58 K), while the non-operability (12–13%) showed little variability with bias. However, choosing to increase the bias to 3 V (where C.E. is maximum) appears to drop the operability to 95.8% and 95.9% at 50 K and 58 K respectively. For the NEdT, it was shown that the population of pixels that are twice the median revealed an operability of 98.8% at 50 K and 98.9% at 58 K. Finally, it was shown that the experimentally measured NEdT values were inadvertently exaggerated from the coupling of an unknown noise source which has yet to be determined. While no dark current mitigation techniques have been applied to this structure, future studies relating to the temperature dependent operability of NEdT histograms are expected to contribute useful knowledge about the applicability of this R-QWIP structure for higher temperature applications.

Conflict of interest

There is no conflict of interest.

Acknowledgments

References

[1] L. Esaki, R. Tsu, Superlattice and negative differential conductivity in semiconductors, IBM J. Res. Dev. 14 (1970) 61.

[2] B.F. Levine, K.K. Choi, C.G. Bethea, J. Walker, R.J. Malik, New 10 μm infrared detector using intersubband absorption in resonant tunneling GaAlAs superlattices, Appl. Phys. Lett. 50 (1987) 1092.

[3] D.L. Smith, C. Mailhiot, Proposal for strained type II superlattice infrared detectors, J. Appl. Phys. 62 (1987) 2545–2548.

[4] E.A. Plis, InAs/GaSb type-II superlattice detectors, Adv. Electron. 2014 (2014).

[5] K.K. Choi, D.P. Forrai, D.W. Endres, J. Sun, Corrugated quantum-well infrared photodetector focal plane arrays, IEEE J. Quantum Electron. 45 (10) (2009).

[6] K.K. Choi, M.D. Jhabvala, J. Sun, C.A. Jhabvala, A. Waczynski, K. Olver, Resonator-quantum well infrared photodetectors, Appl. Phys. Lett. 103 (2013) 201113.

[7] K.K. Choi, M.D. Jhabvala, D.P. Forrai, A. Waczynski, J. Sun, R. Jones, Electromagnetic modeling of quantum well infrared photodetectors, IEEE J. Quantum Electron. 48 (2012) 384.

[8] J. Sun, K.K. Choi, K. Olver, Fabrication of resonator-quantum well infrared photodetector test devices, J. Micro/Nanolith. MEMS MOEMS 13 (1) (2014) 013004.

[9] K.K. Choi, Quantum-well infrared photodetectors and arrays, in: Pallab. Bhattacharya, Roberto. Fornari, Hiroshi. Kamimura (Eds.), Comprehensive Semiconductor Science and Technology, Elsevier, Amsterdam, 2011, pp. 160–228.

[10] B.F. Levine, Quantum-well infrared photodetectors, J. Appl. Phys. 74 (1993) R1–R81.